
Article:
Selkirk, A., Prochukhan, N., Lundy, R. et al. (7 more authors) (2021) Optimization and control of large block copolymer self-assembly via precision solvent vapor annealing. Macromolecules, 54 (3). pp. 1203-1215. ISSN 0024-9297

https://doi.org/10.1021/acs.macromol.0c02543

Optimization and Control of the Self-Assembly Kinetics of a Giant Block Copolymer System via Controlled Solvent Vapour Annealing

Andrew Selkirk,[a,b*] Nadezda Prochukhan,[a,b], Ross Lundy, _____,..... _____, Rachel Kilbride,[c] Andrew Parnell,[c] Jhonattan Baez,[a,b], Mick Morris,[a,b*] Parvaneh Mokarian- Tabari[a,b*]

[a] Advanced Material and BioEngineering Research Centre (AMBER), Trinity College Dublin, The University of Dublin, Ireland.

[b] School of Chemistry, Trinity College Dublin, The University of Dublin, Dublin 2, Ireland.

[c] Department of Physics and Astronomy, University of Sheffield, Sheffield, S3 7RH, UK.

Abstract: The self-assembly of ultra-high molecular weight (UHMW) block copolymers (BCPs) remains a complex and time-consuming endeavor owing to the high kinetic penalties associated with long polymer chain entanglement. In this work, we report a unique strategy of overcoming these kinetic barriers through rapid and controlled solvent annealing of an UHMW lamellae-forming polystyrene-*block*-poly(2-vinylpyridine) BCP system (M_w: ~800 kg mol^{-1}) by fast swelling to very high levels of solvent concentration (ϕ_s). Phase separation on timescales of ~10 minutes is demonstrated once a thickness-dependent threshold ϕ_s value of ~0.80 – 0.86 is achieved, resulting in lamellar features with spacings of over 190 nm. The threshold ϕ_s value was found to be greater for films with higher dry-thickness (D_0) values. Tuneability of the domain morphology is achieved through controlled variation of both the D_0 and ϕ_s, with the kinetically unstable hexagonal perforated lamellar (HPL) phase observed at ϕ_s values of ~0.67 and D_0 values of 59-110 nm. This HPL phase can be induced to undergo an order-order transition (OOT) to a lamellar morphology upon further increasing of ϕ_s to 0.80 or above. The manipulation of the lateral ordering for the lamellar domains is achieved through the variation of ϕ_s. Confirmed by GISAXS, the lateral ordering of the lamellar domains is shown to improve with increasing ϕ_s up to a maximum value at which the films transition to a disordered state. Thicker films are shown to possess a higher maximum ϕ_s value before transitioning to the disordered state. The swelling rate is shown to moderately influence the lateral ordering of the phase-separated structures, while the amount of hold time at a particular value of ϕ_s does not notably enhance the phase-separation process. The self-assembled lamellar domains are then employed to facilitate pattern transfer using a liquid phase infiltration method, generating ordered Si nanowall structures with spacings of ~190 nm, and heights of up to ~500 nm. This

work underpins the feasibility of a room-temperature, solvent-based annealing approach for the reliable and scalable fabrication of sub-wavelength nanostructures via BCP lithography.

Introduction:

The directed self-assembly of block copolymers (BCPs) is a well-studied technique for the controlled formation of a wide range of periodic thin-film morphologies, including spherical, cylindrical, gyroidal, and lamellar among others.[1] Structural modulation can be achieved through the manipulation of the supramolecular composition, while the periodicity of the domains can be adjusted through varying the molecular weight.[2, 3] From a technological standpoint, the high degree of versatility of BCP self-assembly, in addition to ease of scalability and low process temperatures, has provided an attractive route for the fabrication of surface nanostructures with an enormous variety of potential applications, including nanoelectronics,[4] chemical sensors,[5-8] antireflective coatings,[9-12] and optically active surfaces.[13-15] In the case of optical applications such as interconnect patterning, the periodicity of the lateral domain features must generally exceed approximately 100 nm such that the structures are capable of interacting with wavelengths on the order of visible light.[16, 17] In order to facilitate the formation of such feature sizes, ultra-high molecular weight (UHMW) BCP systems with molecular weights in excess of 500 kg/mol are utilised. The self-assembly of such large systems creates additional complexities in the annealing process, in particular the extremely slow ordering kinetics associated with increased chain entanglement.[18] The energy barrier required to induce chain mobility in highly entangled BCPs cannot always be overcome even at temperatures exceeding that of the glass transition temperature T_g of the BCP system, effectively eliminating the possibility of a purely thermal annealing approach in such UHMW systems.[19]

The majority of recent literature, including the work described here, instead employ solvent vapour annealing (SVA) as an alternative technique to facilitate the self-assembly of UHMW systems. SVA involves the uptake of solvent into a BCP film, resulting in increased polymer chain mobility, a lower effective value of the glass transition temperature T_g, and the avoidance of any thermal degradation of the material.[20-22] There are multiple interdependent variables that influence the SVA process, including pressure, temperature and humidity. Nonetheless, previous work has shown it can be performed with a very simple strategy known as 'static' SVA – this consists of a BCP sample placed inside a sealed chamber containing a reservoir of solvent, which is then left for a predetermined period of time.[23-26] Moreover, SVA can be performed at room temperatures or below, and has been proven to effectively induce self-assembly in a number of UHMW BCP systems.[19, 27-30] Kim *et al*. successfully obtained phase-separation of lamellar and gyroid UHMW PS-*b*-PMMA BCP films with periods of ~200 nm using THF as a neutral solvent for SVA, followed by a 12-hour thermal annealing step.[19, 28] Phase separation of an UHMW spherical PS-*b*-PMMA system was also demonstrated by Cao *et al*. again using THF as the annealing solvent of choice.[27] Most recently, Takano *et al*. developed a novel instrumentation technique to monitor the phase separation of UHMW lamellar PS-*b*-PMMA using *in situ* atomic force microscopy (AFM) under high swelling conditions during SVA.[29] Despite the relative success of these previous studies for the induction of phase-separation in UHMW systems, the required timescales often extended from a number of hours to days – thereby hindering the industrial applicability of such processes.[19, 27-29] The acceleration of the SVA process is therefore critical for the future development of this field. Here we demonstrate a procedure for ultrafast fast self-assembly of UHMW block copolymer systems, within minutes of achieving of threshold value for solvent concentration ϕ_s by controlling the swelling kinetics.

One notable improvement in expediting the SVA process for UHMW systems as of late was by Doerk *et al*., who utilised blends consisting of lamella-forming polystyrene-*block*-poly(methyl methacrylate) (PS-*b*-PMMA) ($M_n \leq 2000$ kg/mol) combined with low molecular weight PS and PMMA homopolymer to accelerate the phase separation process. [30] This resulted in the formation of ordered lamellar domains with periodicity of up to 211 nm from a total annealing time of 1 hour (plus an additional 5 min thermal annealing step following SVA). Although this work demonstrated a major step towards accelerated SVA timeframes for UHMW BCPs, the influence of many of the kinetic components of the SVA technique – such as the swelling/de-swelling rate or swelling time – remain predominantly unexplored for such systems. Previous kinetics studies examining lower molecular weight BCPs have proven the critical importance of the aforementioned parameters in the enhancement of self-assembly timescales;[31-35] Hence, it seemed desirable to ascertain the effects of such variables on an UHMW system.

In order to maintain precise control over BCP swelling kinetics during SVA, a variety of specialised annealing chambers have been constructed where the solvent uptake into the BCP film can be regulated *in situ* during annealing.[31, 33, 36-40] The primary kinetic variable of focus for many of these setups is the swollen film thickness D_{sw}, which is dependent on the concentration of solvent inside the polymer film ϕ_s. D_{sw} is well-known to play a crucial role in the kinetics of self-assembly, with a positive observed correlation between a higher value of D_{sw} and increased lateral ordering.[33, 35, 41] In a recent development, Hulkkonen *et al*. utilised a custom-built annealing chamber to precisely control the swelling behaviour of HMW PS-*b*-P2VP systems (($M_n = 258$ kg/mol) via a temperature-controlled sample stage, resulting in the formation of hexagonal cylindrical domains in <15 minutes.[33] The BCP systems examined in this study, however, were not of sufficient molecular weight to fabricate domain sizes greater than 100 nm.

To the extent of our knowledge, little published work exists on optimising the self-assembly kinetics of UHMW BCP systems using controlled SVA techniques.

Accordingly, in this report we investigate the swelling kinetics of a commercially available UHMW lamellar PS-*b*-P2VP BCP system with a molecular weight of ~800 kg/mol (M_n: 440-353 kg/mol, $f_{PS} = 0.57$), in order to improve the reliability and speed of the phase separation process. This particular BCP system was chosen as previous published work by our group demonstrated the potential self-assembly of this system upon exposure to both tetrahydrofuran (THF) and chloroform using the conventional 'static' SVA method.[11] In the work shown herein, we demonstrate a greatly expedited timescale for the phase-separation of UHMW PS-*b*-P2VP films using a custom-built SVA chamber. We firstly examine the effects of the dry film thickness, D_0, and the solvent concentration in the polymer film, ϕ_s, on the structural evolution and lateral grain ordering of the rapidly swollen BCP films, resulting in the controlled formation of both equilibrium and non-equilibrium BCP phases. The formation of the previously demonstrated hexagonal perforated lamellar (HPL) phase along with well-ordered lamellar domains with periods of ~190 nm is achieved using total annealing times of ~10 minutes. The insubstantial effect of the swelling time on the structural evolution, along with the influence of the swelling rate on the lateral grain sizes of the lamellar domains, is also examined. Finally, we also show the capability of the phase separated films to be utilised for pattern transfer, with the formation of sub-wavelength Si nanostructures using a metal salt infiltration process followed by reactive ion etching.

Experimental Section:

Materials & Sample Preparation: Polystyrene-block-poly(2-vinylpyridine) (M_n: 440-b-353 kg/mol, PDI: 1.19) was purchased from Polymer Source Inc. and used without further purification. Anhydrous toluene, tetrahydrofuran (THF) and ethanol were purchased from Sigma-Aldritch and used without further purification. Varying amounts of PS-*b*-P2VP between were dissolved in a 4:1 (volume fraction) blend of toluene and THF to make polymer solutions of between 0.5-3% (w/w), which were left stirring overnight to ensure complete dissolution. For the solvent blend placed inside the bubbler for SVA, chloroform (HPLC, 99.9%) and THF (HPLC, 99.9%) were purchased from Sigma Aldritch and used without further purification. 2×2 cm pieces of Si <100> wafers with a native oxide layer were cleaned using ultrasonication in acetone for 20 minutes, followed by drying under N_2 gas. Polymer solutions were then spin-coated onto the clean Si substrates for 30 seconds at 4500 rpm, and left to dry for 10 minutes at lab temperature.

Annealing Rig: The SVA rig utilized in this study is an upgraded version of the setup described by *Lundy* et al.[36] The stainless steel annealing chamber has an internal volume of 1.94 L, and possesses an access door with a quartz glass viewport located on the top of chamber (see **figure 1**). The inlet and outlet valves for solvent/N_2 vapour flow are located on the left and right-hand side of the chamber respectively. To generate solvent vapour, nitrogen gas was passed through a flow meter and into a bubbler chamber containing the THF-chloroform mixture. In order to maintain a constant vapour pressure inside the SVA chamber over the entire annealing process, it

was essential to mitigate any temperature decrease of the solvent mixture over time due to evaporative cooling. This was achieved by attaching a flexible heat pad to the outside of the solvent bubbler. The heat pad was connected to a PID controller, which maintained a constant solvent temperature of 21.0 $\pm$ 0.15°C using feedback from an RTD probe located inside the bubbler chamber as shown in Figure 1. The flow rate of the N_2 gas was controlled using a gas flow regulator connected to the outlet on the N_2 source, and was maintained at a constant rate of ~400 sccm during annealing. The solvent chamber could be rapidly quenched to preserve the phase-separated BCP morphology using an N_2 gas line that bypassed the solvent bubbler, thus flooding the chamber with pure nitrogen. A copper stage was located inside the chamber on which the samples were placed during annealing, allowing samples of up to 4'' to be processed. An RTD embedded inside the copper stage allowed the stage temperature to be measured, and provided feedback for a PID controller to control the stage temperature (to within an error of $\pm$ 0.15 °C). In order to monitor the film thickness *in-situ* during SVA, a Filmetrics F3-CS reflectometer with a UV-vis light source (380-1050 nm range) was mounted on top of the quartz viewport. To account for any variation in the light source intensity, the reflectometer was calibrated using a Si reflectance standard prior to each sample run. The experimental reflectance data was measured over a wavelength range of 420-1050 nm and used a three-layer model consisting of the Si substrate, the PS-*b*-P2VP BCP layer, and air. Refractive index models for both the dry BCP films and the swollen films were estimated using the Lorentz-Lorentz rule of mixing, which utilized the refractive indices of the pure polymer and solvent components (PS, $n = 1.586$, P2VP: $n = 1.527$, THF: $n = 1.407$, chloroform: $n = 1.440$) to obtain a refractive index range of 1.558 (for the dry BCP film) to 1.457 as the concentration of the THF:chloroform

solvent mixture increased up to a ϕ_s value of 0.87 (**see Section S2)**. The time interval used for each data point shown in this study was 2 seconds, with an integration time of ~250 ms.

SVA process: The BCP samples were placed on the heated copper stage directly under the reflectometer beam, which was baselined prior to each sample measurement as per above. The initial stage temperature, which ranged between (15.9 °C and 20.9 °C) depending on the experiment, was set prior to initiating the annealing process. Solvent vapour was firstly allowed to flow into the chamber at a constant rate of 400 SCCM during which the film thickness and annealing time were recorded by the reflectometer. Once the sample approached the desired swollen thickness, the temperature of the stage was gradually increased in increments of 0.1 °C using the PID controller to slow the swelling rate to zero. The film was then held at this swollen thickness value for the required annealing time of the experiment. During the hold time, the stage temperature was periodically adjusted in increments of 0.1 °C to avoid any large fluctuations in the film thickness. As soon as the required hold time was reached, the temperature of the stage was instantaneously increased to 30 °C and the chamber was purged with nitrogen, which ensured a rapid deswelling regime (of approximately 5-10 seconds depending on the swollen thickness) and that all remaining solvent inside the film was purged.

Oxide nanostructure formation, pattern transfer: The formation of the metal oxide structure from the BCP template follows a similar process described in previous work. Samples were first immersed in ethanol for 20 minutes to facilitate surface reconstruction, and subsequently left to dry at room temperature. Iron (III) nitrate nonahydrate ($Fe_2(NO_3)_3.9H_2O$) was dissolved in ethanol at a concentration of 0.5 % w/w, and nickel (II) nitrate hexahydrate ($Ni(NO3)_2.6H_2O$) was dissolved in ethanol at a concentration of 0.6% w/w. The salt solution was

stirred for 1 hour to ensure complete dissolution and was then spin-coated onto the ethanol-reconstructed BCP samples at a speed of 3200 RPM for 30 seconds. A UV/O_3 treatment (PSD Pro Series Digital UV Ozone System; Novascan Technologies, Inc.) was then performed on the samples for 3 hours to completely remove the polymer template and oxidize the metal precursor. Pattern transfer was performed using an Oxford Instruments Plasma Technology Plasma lab System100 ICP800 etcher, with a gas mixture of SF_6 (15 sccm) and CHF_3 (80 sccm), an ICP power of 1200 W and RIE power of 20 W, and a chamber pressure of 20 mTorr.

Sample characterisation: Atomic force microscopy (AFM) was performed in non-contact mode (Park Systems, XE-7 under ambient conditions using silicon cantilevers (PPP-NCHR model) with a force constant of 42 N/m. SEM images were taken using a Carl Zeiss Ultra plus using the InLens detector with an accelerating voltage of 5 kV and a working distance of 4.5 mm. For cross-sectional SEM images, the substrate was cleaved into two and placed on a sample holder that was angled perpendicular to the electron beam. The stage was then tilted to between 10-20°, depending on the image. Grazing Incidence Small Angle X-ray Scattering (GISAXS) was performed at the Soft Matter Analytical Laboratory (SMALL), Department of Chemistry, University of Sheffield using a Xeuss 2.0 (Xenocs) system with 9.243 keV X-rays from a liquid Ga MetalJet source (Excillum), with an incident beam angle of 0.16°.

Image analysis: Orientational mapping was performed on SEM images using the OrientationJ plugin for ImageJ. The correlation length, an indicator of orientational ordering in the pattern, was estimated using software described by Murphy *et al*.,[42] where the correlation function is obtained from a set of orientation angles that are calculated using a skeletonization process on the BCP domain structures of each image. 10×10 μm AFM images were used to determine the

correlation length values shown in this report (example in **Figure S10**). To briefly describe the process, the contrast between the two BCP domains (in this case the PS and P2VP domains) is firstly enhanced though smoothing (to reduce random noise) and then converted into a binary image by thresholding (PS represented as black, P2VP white). The line features identified from the binary images are then skeletonized into single-pixel width, and the orientational angle $\phi(r)$ of each pixel along the skeletonized line features is determined using a rolling average of the tangent along each line. The correlation function $C(r-r')$ can then be calculated from the set of orientation angles $\phi(r)$ for each point analyzed in the image as follows: $C(r-r') = \langle \cos[2\{\phi(\mathrm{r}) - \phi(\mathrm{r}')\}] \rangle$. The correlation length ξ is then related to the correlation function through an exponential fit: $C(r-r') = e^{-\frac{r}{\xi}}$. All error bars in this work represent two standard deviations (2σ) from the mean value unless stated otherwise.

Results and Discussion:

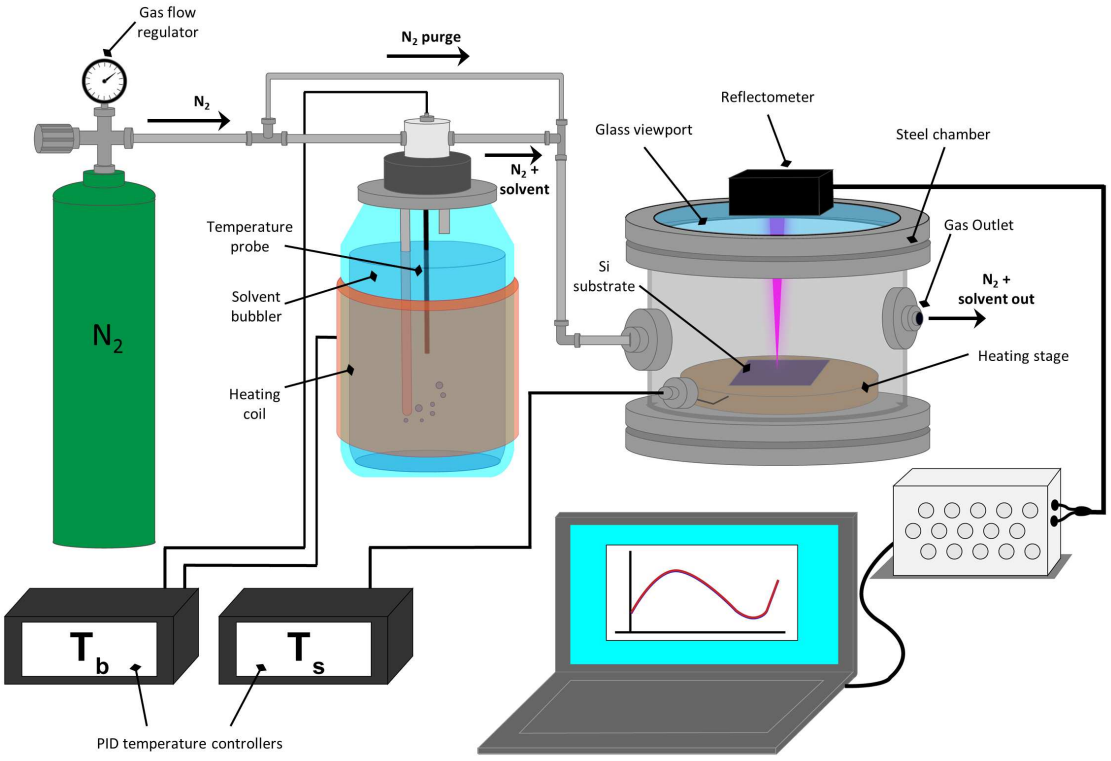

Figure 1: Diagram of the annealing setup. Films of PS-*b*-P2VP are spin-coated onto Si substrates, and then annealed inside the chamber while the film thickness is monitored *in situ* using a reflectometer.

A 793 kg/mol PS-*b*-P2VP (440 kg/mol PS, 353 kg/mol P2VP) BCP was utilized for this study. This system was of particular interest, as it was shown in previous work by our group to be capable of phase separation into a kinetically unstable HPL structure upon SVA in a THF and chloroform atmosphere for an hour, with feature spacing of ~180 nm.[11] This structure, with large area coverage and sub-wavelength periodicity, proved to be highly applicable in the fabrication of antireflective nanostructures. One issue that was encountered, however, was the low reproducibility of the self-assembly method. It was found that slight fluctuations in the lab temperature, annealing solvent concentration, or even the position of the sample within the annealing chamber often led to widely different morphologies than what was desired. Although the variation in results was expected due to the non-equilibrium nature of microphase separation UHMW BCPs, it was of interest from a technological point of view to examine and monitor the self-assembly kinetics in more detail in order to achieve greater repeatability.

UHMW BCP systems typically require high swelling ratios in order to initiate polymer mobility.[43] This is due to the influence of molecular weight on the level of chain entanglement – higher molecular weight systems possess longer polymer chains, and thereby a higher degree of entanglement in the dry BCP film. SVA is a well-known method that can be used to address this issue. In the case of the addition of a relatively neutral solvent to the BCP film via SVA, the polymer-polymer interactions can be reduced as the solvent molecules produce a screening effect at the interface between the two blocks.[44] This screening effect can be quantitatively represented by an effective interaction parameter χ_{eff}:[45]

$$\chi_{eff} = \chi\phi_{BCP}^{\beta} \#(1)$$

Where χ is the Flory-Huggins interaction parameter for the dry BCP film, ϕ_{BCP} is the polymer concentration of the swollen film, and β is an exponent factor with a value that varies between ~1 to ~2, and varies depending on the morphology of the ordered film, the selectivity of the solvent, and the solvent concentration inside the film.[46, 47] A higher swelling ratio (and consequently a lower value of ϕ_{BCP}) will therefore reduce the value of χ_{eff}, increasing chain mobility and allowing phase separation to occur. ϕ_{BCP} is equal to (D_0/D_{sw}), the inverse of the swelling ratio, where D_0 is the initial film thickness, and D_{sw} is the swollen film thickness. This value can also be related to the solvent concentration inside the BCP film, ϕ_s, which is equal to $1-\phi_{BCP}$.

Conventional SVA methods are often incapable of attaining the minimum swelling ratio required to initiate phase separation of UHMW systems regardless of the total annealing time, due to a lack of control over the relative saturation P/P_{sat} of the solvent vapour in the chamber (where P is the partial pressure of the annealing solvent vapour and P_{sat} is the saturated vapour pressure of the solvent at a fixed temperature).[33] Control over the relative saturation of a BCP film during SVA is crucial in order to attain high swelling ratios, as P/P_{sat} is directly related to ϕ_{BCP} through the following relationship:[48]

$$\ln\left(\frac{P}{P_{sat}}\right) = \chi(\phi_{BCP})^2 + \ln(1-\phi_{BCP}) + (1-N^{-1})(\phi_{BCP}) \#(2)$$

Consequently, in order to fully examine the swelling kinetics of the UHMW BCP system, we utilized a customized SVA rig system where the P/P_{sat} of the annealing chamber (and thereby the ϕ_{BCP} value at any given time) could be carefully monitored *in-situ* by varying the temperature of the sample stage ($\pm$ 0.1 °C) as shown in **Figure 1.** By incrementally decreasing

the temperature of the stage, the P/P_{sat} in the localized area of the BCP film is increased leading to a greater degree of solvent uptake. Conversely, if the stage temperature is increased, the P/P_{sat} will decrease inducing solvent expulsion from the film.[33, 36] This setup is an upgraded version of the system described by *Lundy* et al, with the addition of a reflectometer that allows *in-situ* monitoring of film swelling.[36] The various kinetic parameters of the film swelling experiments such as the swelling ratio, swelling time, or rate of swelling, were controlled through precise variation of the stage temperature ($\pm$ 0.1 °C), while maintaining a constant solvent temperature of 21.0 $\pm$ 0.1 °C in the

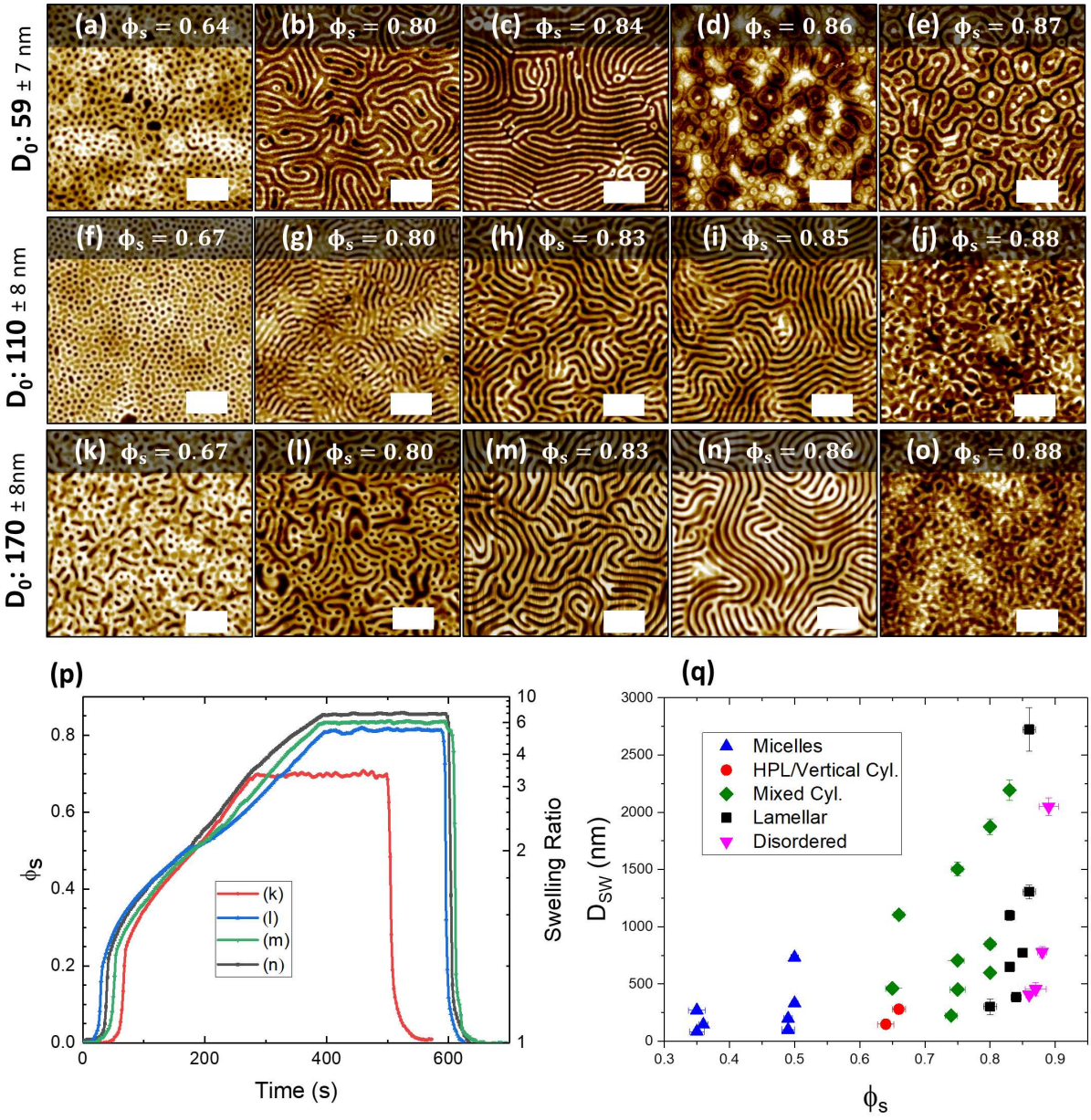

Figure 2: AFM images (a)-(o) show PS-*b*-P2VP films of varying thicknesses annealed in 2:1 chloroform:THF vapour up to a range of solvent concentration (ϕ_s) values . Once the targeted value of ϕ_s was reached, the films were held at this value for approximately 200s before being rapidly quenched in order to preserve the phase-separated structure. (p) solvent uptake during SVA, with the corresponding ϕ_s value shown inset that the film was held at for 200s. (q) is an orientation diagram of the swollen film thickness D_{sw} as a function of

ϕ_s, with the colour of each data point conveying the resulting morphology of the film post-SVA. Scale bars are 1 μm.

bubbler. The noted degree of accuracy for the stage temperature is essential for the controlled swelling of BCP films to high values of ϕ_s, as even minute fluctuations in sample temperature at high swelling regimes can result in dramatic variations in the swollen film thickness.[33] The setup was contained in a fume hood that was maintained at a lab temperature of ~21 $\pm$ 1 °C. By decreasing the temperature of the stage, the relative saturation of the solvent vapour was increased, hence increasing the swelling ratio of the film.[22]

The annealing solvent of choice for this study was a blend of THF and chloroform, both of which are relatively non-selective to both PS and P2VP segments (slight selectivity of THF to PS, and chloroform to P2VP).[35, 48] A range of solvent blend ratios were trialed in order to optimize the phase separation of the BCP system (See **Section S1**), of which a 2:1 molar ratio of chloroform to THF was chosen as the optimal blend ratio for the kinetic studies described below. This was calculated to give a ratio of approximately 82:18 of chloroform to THF in the vapour phase, due to the non-ideality of the solvent mixture.[49] Both THF and chloroform have high vapour pressures with values that are relatively close at 21 °C (136 mmHg and 165 mmHg respectively, see **Section S1**), therefore it was assumed that the mole fractions of both solvents within the bubbler did not vary significantly over the annealing timescales analyzed in this work. A full description of the solvent variation experiments, including AFM images of samples along with a calculation of the resulting vapour phase mole fractions accounting for the nonideality of the mixture, is contained in the **SI.** A more detailed analysis of the effect of solvent mixtures will be the subject of a future study.

As a starting point for this kinetic study, we decided to examine the effects of varying both D_0 and ϕ_S on the resulting phase-separated morphologies of the BCP system. **Figure 2a-l** shows a set of AFM images of the PS-*b*-P2VP BCP film annealed as a function of both D_0 and ϕ_s. The value of D_0 was varied by adjusting the concentration of the BCP dissolved in solution prior to spin-coating (from 1 to 3% w/w), giving an initial thickness range of ~ 59 to 371 nm. The films were swollen to a range of ϕ_S values and held at the set value for 200s before rapid deswelling through N_2 purging of the chamber. The temperature conditions for the films were kept as constant as possible to ensure the swelling rate remained similar for all films, with an initial stage temperature of 19.9 ℃ and a bubbler temperature of 21.0 ℃. Some slight variation in swelling profiles between samples is noted (**Figure 2p**), which we attribute to minor daily temperature fluctuations in the lab environment. To avoid any excessive fluctuation in ϕ_s during the 200s hold time, the stage temperature was manually varied in increments of ± 0.1 ℃. The total annealing times were between ~ 8 – 11 minutes, with samples held at higher ϕ_s values requiring slightly longer swelling times as shown in the example set of *in-situ* swelling plots for the 170 nm films (**Figure 2p).**

A significant evolution of the film morphology was observed as the value of ϕ_s that the films were held at was increased. Below a ϕ_s value of ~ 0.64, no apparent structural change was observed for any value of D_0, with the films remaining in an apparent vitrified micellar state as seen in previous studies.[37, 41] At ϕ_s values of between ~ 0.64 to 0.67, as can be seen in **Figures 2a, e**, a perpendicular cylindrical surface structure emerged for D_0 values of ~ 59 and 118 nm. We suggest that this is a hexagonally perforated lamellar (HPL) structure, as we previously observed through static SVA of this system.[11] The formation of the HPL phase is attributed to confinement effects as the film thickness decreases below L_0, and the limited maneuverability of

the polymer chains at low values of ϕ_s.[50] As the thickness of the unswollen dry BCP film moves toward commensurability ($D_0 \geq \sim 166$ nm), as was the case in **Figure 2i**, the HPL phase was not observed at the same ϕ_s values and

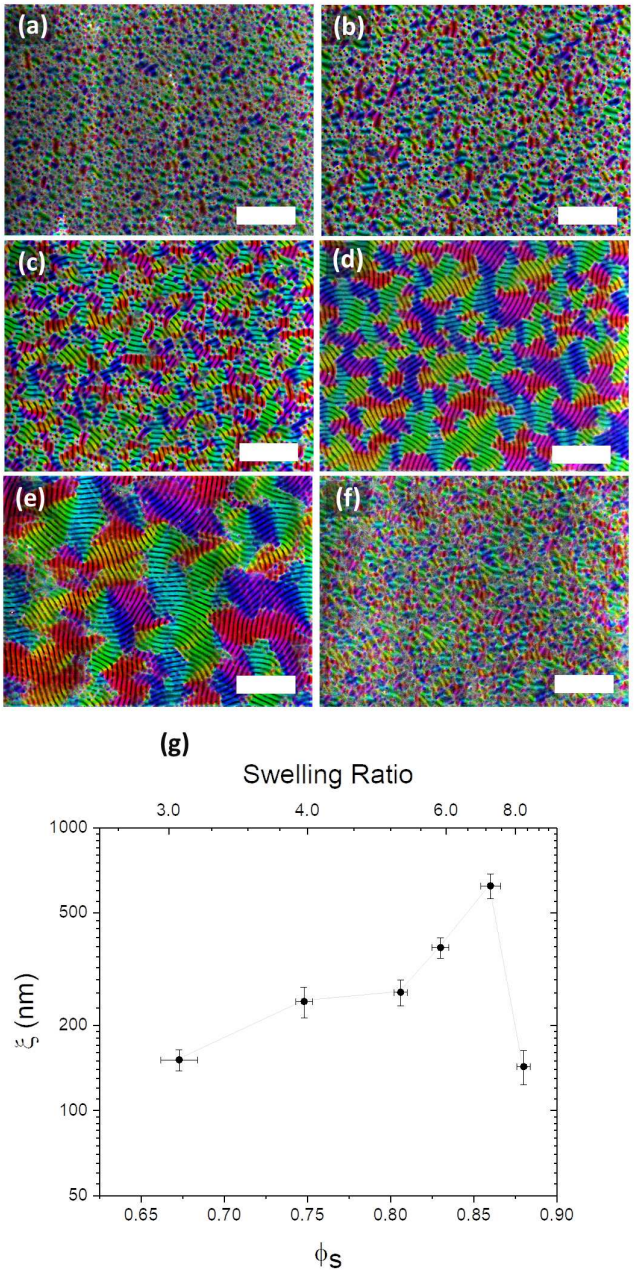

Figure 3: (a)-(d): Orientational mapping of SEM images showing grains parallel to the surface after swelling to different values of solvent concentration (ϕ_s): (a) $\phi_s = 0.67$, (b) $\phi_s = 0.75$, (c) $\phi_s = 0.80$, (d) $\phi_s = 0.83$, (e) $\phi_s = 0.86$ (f) $\phi_s = 0.88$, (g) correlation length ξ as a function of ϕ_s and the swelling ratio. Scale bars are 2 μm.

a mixed cylindrical structure was instead noted. As ϕ_s was further increased to ~ 0.80 to 0.87, well-developed lamellar structures were observed to emerge at all D_0 values. The domain period L_0 of these structures was determined to be 193 nm from power spectrum density (PSD) plots of AFM images **(See Figure S7).** Interestingly, we noted a slight correlation between the critical ϕ_s value at which the onset of phase separation occurred ($\phi_{s,c}$) and D_0, with the onset shifting toward lower $\phi_s$values for thinner films. This is likely due to a reduction in the amount of entangled material required to rearrange at lower D_0 values, which has been shown in previous work to result in faster ordering kinetics.[51] We attribute the high observed value of $\phi_{s,c}$ to the larger chain lengths and subsequent high level of entanglement associated with this UHMW system. In the case of the films with $D_0 = 59 - 118$ nm, the HPL phase was observed to undergo an order-order transition (OOT) to a lamellar structure (**Figures 2b, f)** upon increasing ϕ_s, in agreement with previous work.[52] The ordering of the lamellar domains increased with increasing ϕ_s up to a D_0-dependent value of ~ 0.86 to 0.88, upon which the films seemed to undergo an order-disorder transition (ODT) with the disappearance of any observable surface ordering. Again, a thickness dependence was observed for the value of ϕ_s at the ODT (henceforth referred to as $\phi_{s,ODT}$), with lower D_0 resulting in a slightly lower $\phi_{s,ODT}$. A likely

explanation for this dependence is the reduction in polymeric material resulting in less required molecular rearrangement as mentioned previously. The effect of ϕ_s on the lateral ordering is more closely examined below in **Figure 3**. The complete range of ϕ_s values and their resulting morphologies are summarized in the orientation diagram shown in **Figure 2n**, with their corresponding AFM images available in **Figure S8**.

In order to quantify the effect of ϕ_s on the lateral ordering of the lamellar features, we used image analysis software to generate orientation maps of the BCP films after SVA. **Figure 3a-f** shows colorized SEM images of the PS-*b*-P2VP films with $D_0 = \sim 166$ nm swollen to and held at various values of ϕ_s $(0.67 - 0.88)$ for 200s followed by rapid deswelling (same annealing conditions as F**igure 2**), with the coloring representing the orientation of the lamellar microdomains. The orientational ordering of the films increases with the ϕ_s value reached during swelling, with significant microdomain orientation only observed at $\phi_s = \sim 0.83$ or higher. The maximum grain size was achieved at $\phi_s = \sim 0.86$, with complete disordering of the phase-separated lamellar structure observed at $\phi_s = \sim 0.88$. The ODT value of ϕ_s can therefore be cautiously estimated to lie close to the value of $\phi_s = \sim 0.87$. The grain size was further quantitatively characterized by determining the microdomain correlation length ξ for the lateral ordering of the lamellar structures for each sample, shown in **Figure 3g**, using automated defect analysis software as described by *Murphy* et al.[42] At low levels of ϕ_s, the value of ξ remains at a value close to the domain period of ~190 nm. The highest value of $\xi = 723 \pm 62$ nm was obtained through annealing at the closest possible ϕ_s value (0.86) to our estimated ODT concentration of $\phi_s = \sim 0.87$. Once the swelling surpassed this point, as was the case with **Figure 3f** where $\phi_s = 0.88$, long range ordering was lost and the value of ξ returned to the order of roughly a single domain period.

GISAXS was then used to examine the effect of ϕ_s on the internal structure of the 170 nm BCP films over macroscopic areas. Measurements were taken of the films after rapid deswelling with no subsequent processing, as shown in the GISAXS images in **Figures 4a-h** along with the 1D in-plane intensity profiles in **Figure 3i**. The 1D intensity profiles were extracted from the GISAXS images at the determined Yoneda position for each sample. A clear evolution of morphology can be observed as ϕ_s increases. For the as-cast film, a very weak scattering pattern is evident in **Figure**

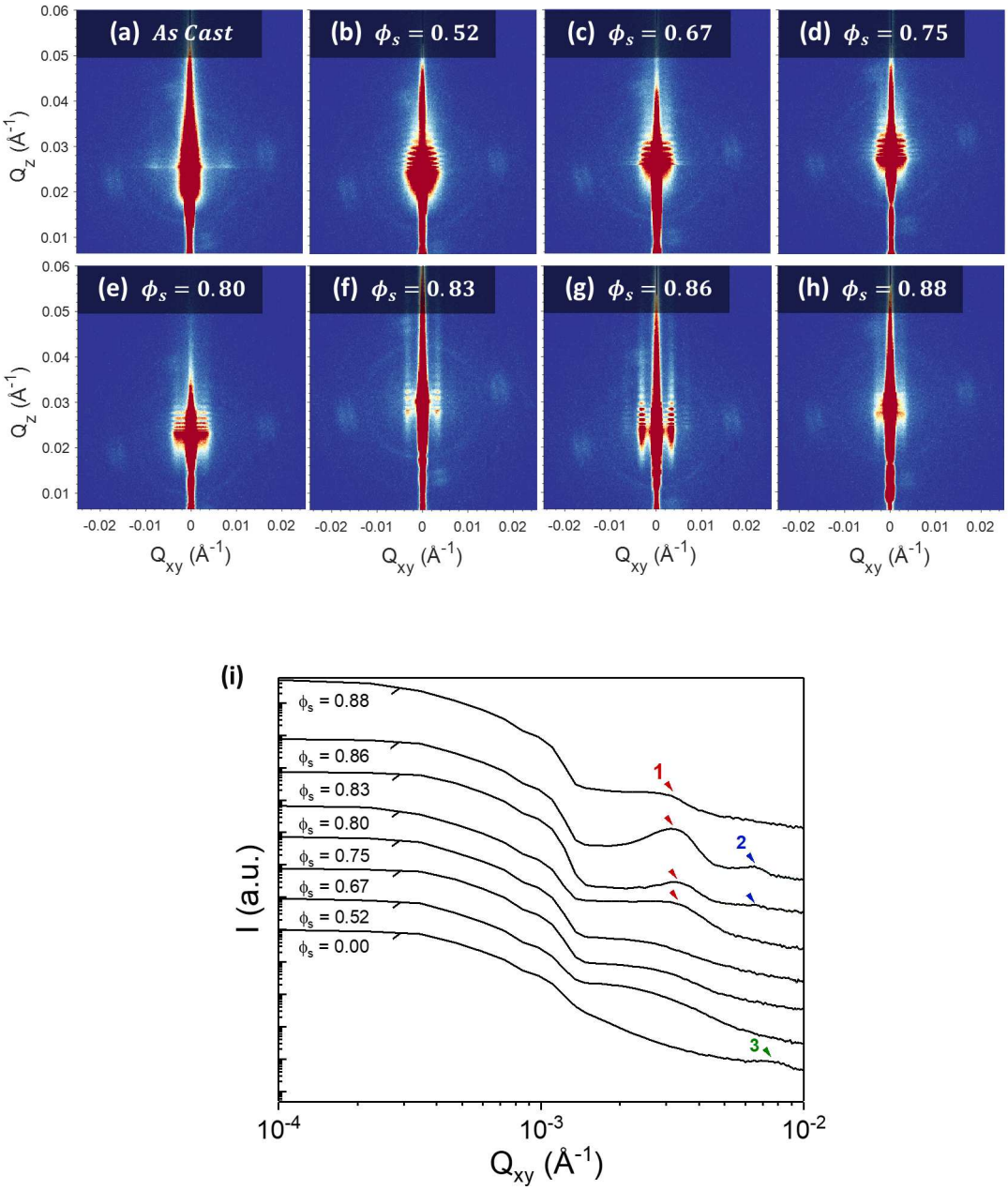

Figure 4: (a)-(h): 2-dimensional GISAXS scattering patterns showing the morphological evolution of the 166 nm PS-*b*-P2VP films swollen to different values of ϕ_S. Films were held at the noted value of ϕ_s for ~ 200 s before rapid deswelling. (ϕ_s): (a) $\phi_s = 0.67$, (b) $\phi_s = 0.75$, (c) $\phi_s = 0.80$, (d) $\phi_s = 0.83$, (e) $\phi_s = 0.86$ (f) $\phi_s = 0.88$, (g) correlation length ξ as a function of ϕ_s and the swelling ratio. First order, second order scattering peaks are marked as 1 and 2, and scattering peak for as-cast micelle film as 3. Scale bars are 2 μm.

4a – this indicates a mainly disordered film, which can be attributed to the kinetically-trapped state after rapid solvent evaporation during spin-coating.[53] A weak scattering peak is evident in **Figure 4i** (marked as 3) at a Q_{xy} value of ~ 2.98×10^{-3} $Å^{-1}$, which corresponds to a domain spacing d of ~79 nm (using $d = \frac{2\pi}{Q_{xy}}$); this likely originates from the micellar structures evident in AFM images of the as-cast film surface **(**shown in **Figure S7).** For films swollen to a ϕ_s value of between 0.52 to 0.75 (**Figure 4b-d**) no notable scattering peaks are observed, which suggests that the BCP chains are still too entangled at this level of swelling to self-assemble into well-defined microdomains. Upon reaching a ϕ_s value of 0.80 (**Figure 4e**), a first-order scattering peak (marked as 1) begins to emerge at a Q_{xy} value of approximately 3.33×10^{-3} $Å^{-1}$. This peak sharpens and intensifies in strength along Q_z as ϕ_s is increased to 0.83 and then to 0.86 (**Figure 4f, g**) indicating a structural transition to a perpendicular lamellar morphology once the films exceed the threshold ϕ_s value of ~ 0.8. The in-plane domain spacing d at $\phi_s = 0.83$ is calculated to be approximately ~184 nm ($Q_{xy} = 3.41\times10^{-3}$ $Å^{-1}$), while at $\phi_s = 0.86$ this increases to 191 nm ($Q_{xy} = 3.29\times10^{-3}$ $Å^{-1}$). These values are in close agreement with lamellar spacings calculated from AFM images **(see Figure S8).** A weak second order peak is also visible at $2Q_{xy}$* (marked as 2), which again is indicative of the development of well-ordered perpendicular lamellar domains in the film.[54] Once the value of ϕ_s is increased to 0.88 (**Figure 4h**), the first order peak is observed to diminish. This insinuates a loss of structural ordering throughout the BCP film as it undergoes an ODT, which is in agreement with the surface transition shown in AFM images **(Figure 2n, o**). Oscillations in Q_z can be observed for all ϕ_S values between 0.52

to 0.86, which we suggest arise from surface roughness correlation effects between the polymer film and the substrate.[55]

In order to fully optimize and understand the annealing process, it was essential to determine the

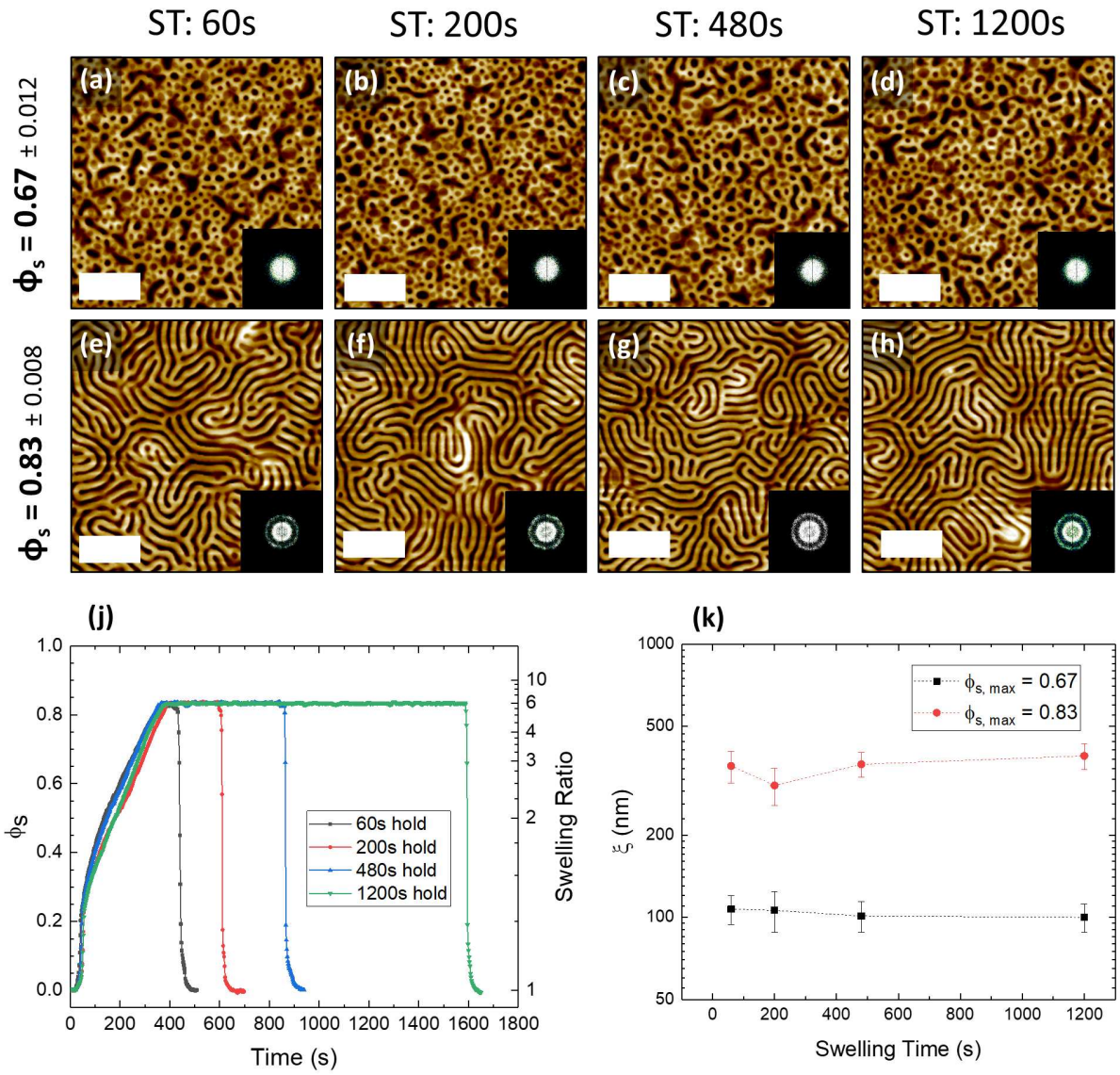

Figure 5: AFM images (a)-(d) show PS-*b*-P2VP films annealed to a solvent concentration (ϕ_s) value of 0.67 and held at this value for different amounts of time (ST = 60, 200, 480 and 1200 seconds). (e)-(h) are annealed to $\phi_s = 0.83$ and held for the same timescales. Corresponding Fourier transforms are shown inset. (j)

shows the swelling profiles for (e)-(h), as a function of ϕ_s and swelling ratio. (k) shows the variation of the correlation length ξ with swelling time. All scale bars are 1 μm.

effect of the annealing time on the relative ordering and morphologies of the BCP films. A series of BCP films with a D_0 value of ~170 nm were swollen to either ~ $3D_0$ ($\phi_s = 0.67$) or ~ $6D_0$ ($\phi_S = 0.83$), and held at that swelling ratio for varying amounts of time between 60-1200 seconds, as shown in **Figure 5**. The rate of swelling was maintained by controlling the stage and bubbler temperatures, along with a constant N_2 flow rate of ~400 sccm**.** For both values of ϕ_s, it was observed that the amount of time the BCP was held at a particular solvent concentration did not significantly affect the morphology or ordering of the resulting structure. In the case of **Figure**s **5a-d,** where the films were swelled to $3D_0$, the increased swelling time did not result in a more ordered or developed structure. This is furthermore confirmed by the low level of variation in the value of ξ in **Figure 5k.** In the case of the films swelled to $6D_0$, phase separation was induced but again, the increase in swelling time did not result in any observed increase in lateral ordering, and the value of ξ remained with the range of approximately 300-400 nm. These results reinforce the existence of a minimum $\phi_{s,c}$ value, below which the BCP films will remain in a vitrified state regardless of the annealing time.[56] This observation is also in agreement with previous work on lower molecular weight cylinder-forming PS-*b*-P2VP systems that showed minimal change in the ξ with longer annealing times.[41]

The influence of the swelling kinetics was further examined through varying the rate of swelling as solvent was uptaken into the films. This was achieved by setting different values of the stage temperature (between 15.9 – 20.9 °C, see **Figure S6**) during the initial solvent uptake component of the annealing, with a constant bubbler temperature and N_2 flow as before. **Figure 6** shows

AFM images of the BCP film with the same D_0 value of ~170 nm annealed to approximately ~$5D_0$ ($\phi_s = 0.80$) or ~$7D_0$ ($\phi_s = 0.86$). The swelling rate was measured as the change in solvent concentration

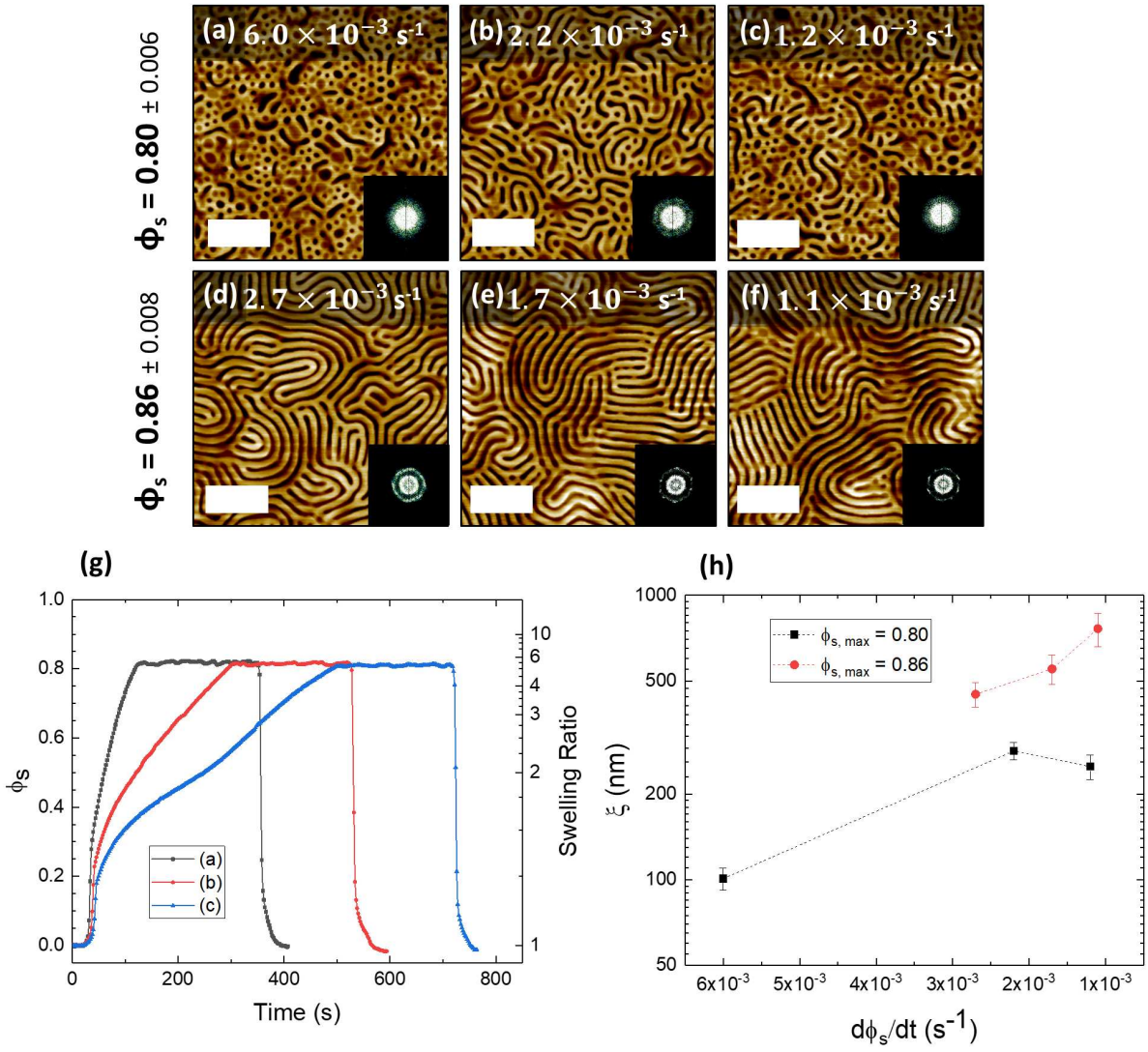

Figure 6: The effect of swelling rate $\left(\frac{d\phi}{dt}\right)$ on lateral ordering for two different values of ϕ_s**.** AFM images of films with different swelling rates for film reaching $\phi_s = 0.8$ **(a)-(c)**, $\phi_s = 0.86$ (d)-(f). Fourier transforms

are shown in the insert. (g) solvent annealing profile for (a)-(c) as a function of ϕ_s and swelling ratio at different swelling rate. (h) correlation length ξ at different swelling rate, indicating the slower swelling rate improves the micro-domain correlation length. All scale bars are 1 μm.

inside the BCP film over time, $\frac{d\phi_s}{dt}$, and was calculated by fitting a linear regression model to the metered solvent uptake regime of the plots (example plots shown in **Figure 6g)**, ignoring the initial solvent uptake regime between ϕ_s values of $0 - 0.25$.[37] Once the desired film thickness was reached, minor adjustments were made to the stage temperature in order to maintain a constant thickness value for ~200 seconds, before rapid deswelling.

In the case of **Figure 6a-c,** where the films were swelled to a ϕ_s value of 0.8, the rate of swelling was varied from 1.2×10^{-3} s^{-1} to 6×10^{-3} s^{-1}. No significant structural change was observed as the value of $\frac{d\phi_s}{dt}$ was varied, and the BCP films remained in the region of the partially self-assembled state. A slight improvement in the calculated value of ξ is observed for films with $\phi_s = 0.8$ in **Figure 6h**. **Figures 6d-f** show improvement in ordering as the swelling rate decreased from $2.7\times10^{-3}s^{-1}$ to 1.1×10^{-3} s^{-1}, with the value of ξ increasing from 449 nm up to 724 nm. It should be noted that the range of swelling rates examined for the $\phi_s = 0.86$ sample set is smaller than for $\phi_s = 0.8$. This is because it was found that our reflectometer model began to fail at swelling rates that exceeded approximately 3×10^{-3} s^{-1} for the films swollen to $\phi_s = 0.86$. We suggest that this may be the result of increased macro-scale film roughness caused by the rapid and non-uniform absorption of solvent into the film during a fast initial swelling regime, which is likely exacerbated at higher ϕ_s values. This established an experimental limit for the highest possible swelling rate shown in this work. It may be feasible to

further accelerate the self-assembly process with a more uniform solvent distribution system in the chamber, or different instrumentation to account for a large roughness factor during the in-situ measurement of film thickness.

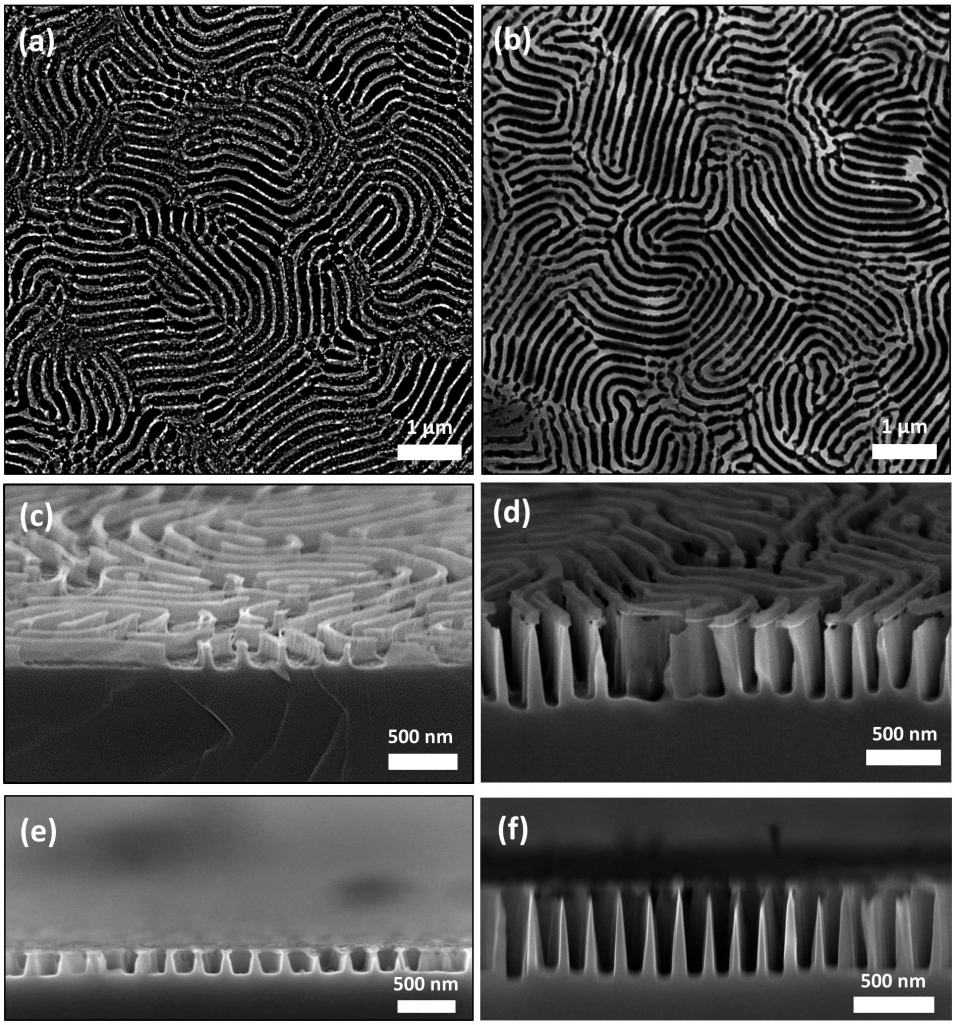

Figure 7: SEM images of Si nanowall after pattern transfer. Top-down SEM images of Si nanowall structures following an ICP etch of the iron oxide hardmask for (a) 1 minute, and (b) 3 minutes, with (20°) tilted images shown in (c), (d) respectively. (e), (f) show cross-sectional SEM image of Si nanowalls for samples (a) and (b).

In order to demonstrate the pattern transfer capability of the self-assembled films, a liquid phase metal salt infiltration process followed by UV/O_3 treatment (to remove the polymer matrix) was performed to convert the BCP film into template for the formation of metal oxide nanostructures. This type of hard mask fabrication process has proven highly successful in previous work for manufacturing a variety of Si nanostructures.[11, 57, 58] The metal oxide templates were then used as a etch mask, and the samples were etched for a range of times via an ICP-RIE etching technique using CHF_3 and SF_6 gases. In the case of samples with etch times of up to 1 minute, an iron oxide hardmask was employed via infiltration of iron nitrate ($Fe(NO_3)_2$), while for etch times of up to 3 minutes a nickel oxide mask (from a nickel nitrate precursor) was instead used. This is because it was found that the nickel oxide mask was more durable over the longer etch times and resulted in less structural degradation and higher etch contrast. **Figure 7a-d** show SEM images of the resulting Si nanowall structures after 1 minute and 3 minutes, demonstrating a high degree of homogeneity

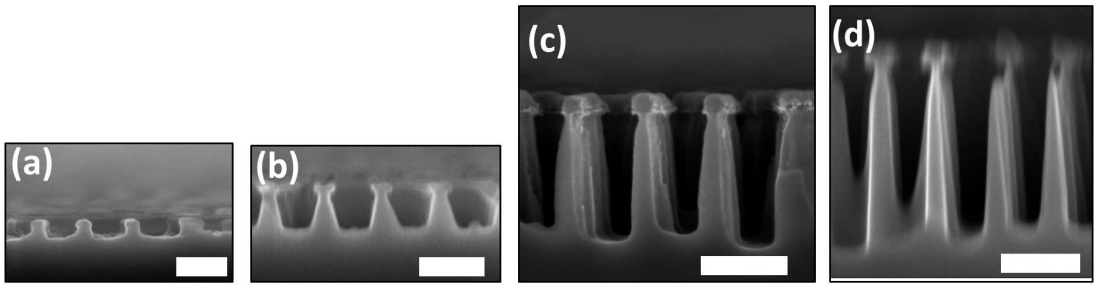

Etch time (s)	30	60	120	180
Height (nm)	78	145	373	493

Figure 8: High resolution cross-sectional SEM images of Si nanowalls, after (a) 30 seconds, (b) 60 seconds, (c) 120 seconds, and (c) 180 seconds of etch time. The table shows the variation of feature heights with etching time. All scale bars are 200 nm.

over the sample surfaces. **Figures 7e, f** show cross-sectional SEM images of the Si nanowall features, again showing uniform nanowall structures with feature spacings of ~ 190 nm and heights of ~ 145 and ~ 493 nm respectively. A summary table of the variation of feature heights with etch time is displayed in F**igure 8**, along with high-resolution cross-sectional SEM images of the nanowall structures.

Conclusion:

In order for BCP lithography to become a viable candidate for the fabrication of large period (>100 nm) nanostructures, it is critical for the self-assembly of UHMW systems to be enhanced for maximal structural control and minimal annealing time. We studied the swelling kinetics of an UHMW BCP system through the use of a temperature-controlled solvent annealing rig, allowing for precise control over the pattern structure, ordering, over a very short period of annealing time. We show that at very high levels of solvent uptake ($\phi_s \geq 0.8$), where the polymer concentration is close to the experimentally estimated ODT point, it is possible for an UHMW BCP system to undergo rapid phase separation into lamellar domains of 190 nm spacing on timescales of 10 minutes. As supported by GISAXS analysis, the closer the value of ϕ_s becomes to the observed $\phi_{s,ODT}$ value, the higher the lateral ordering of the film. The thickness of the dry BCP film was found to positively correlate with both the minimum ϕ_s value required to initiate self-assembly, along with the observed ODT value of ϕ_s. Furthermore, when the dry film thickness was modulated in conjunction with ϕ_s, the domain morphology could be induced to obtain the kinetically unstable HPL phase at a thickness close to half that of the domain

period.[11] The amount of time a polymer film is held at a particular value of ϕ_S during SVA is shown not to ostensibly impact the ordering or domain structure. The rate of swelling, on the other hand, exhibits a moderate influence on the domain ordering for ϕ_s values that are sufficiently high to induce phase separation, with slower swelling rates resulting in improved lateral ordering. It should be noted that the optimization of lateral ordering was somewhat limited by the temperature sensitivity of our annealing setup; we anticipate that future studies may achieve even higher degrees of ordering through controllably approaching the ODT point with greater accuracy. The domain structures obtained from these self-assembled BCP films were easily utilized for pattern transfer through metal salt inclusion, with the formation of metal oxide hard masks that were etched to create uniform and regular arrays of high aspect ratio Si nanowall features.

In conclusion, the results of this study demonstrate that a considerable reduction in the annealing time of UHMW BCP systems is possible using a carefully regulated SVA-based approach, improving upon previous work that typically required high temperature annealing and/or timescales on the order of hours or days.[19, 27-29] The speed and reliability of this technique represents a major step towards a cost-effective and scalable strategy for the fabrication of optical nanostructures such as 2D photonic crystal structures[59, 60] using BCP lithography, with feature spacings on the order of visible light.

Acknowledgement. To be added later

Bibliography

1. F. S. Bates and G. H. Fredrickson, *Annual Review of Physical Chemistry*, 1990, **41**, 525-557.
2. M. W. Matsen and F. S. Bates, *Macromolecules*, 1996, **29**, 7641-7644.
3. C. Park, J. Yoon and E. L. Thomas, *Polymer*, 2003, **44**, 6725-6760.
4. C. Cummins, T. Ghoshal, J. D. Holmes and M. A. Morris, *Advanced Materials*, 2016, **28**, 5586-5618.
5. A. Subramanian, G. Doerk, K. Kisslinger, D. H. Yi, R. B. Grubbs and C.-Y. Nam, *Nanoscale*, 2019, **11**, 9533-9546.
6. S. Z. Bas, C. Cummins, A. Selkirk, D. Borah, M. Ozmen and M. A. Morris, *ACS Applied Nano Materials*, 2019, **2**, 7311-7318.
7. Z. Harandizadeh and T. Ito, *ChemElectroChem*, 2019, **6**, 5627-5632.
8. Y. S. Jung, W. Jung, H. L. Tuller and C. A. Ross, *Nano Letters*, 2008, **8**, 3776-3780.
9. X. Li, L. Xue and Y. Han, *Journal of Materials Chemistry*, 2011, **21**, 5817-5826.
10. S. H. Mir, G. Rydzek, L. A. Nagahara, A. Khosla and P. Mokarian-Tabari, *Journal of The Electrochemical Society*, 2019, **167**, 037502.
11. P. Mokarian-Tabari, R. Senthamaraikannan, C. Glynn, T. W. Collins, C. Cummins, D. Nugent, C. O'Dwyer and M. A. Morris, *Nano Letters*, 2017, **17**, 2973-2978.
12. A. Rahman, A. Ashraf, H. Xin, X. Tong, P. Sutter, M. D. Eisaman and C. T. Black, *Nature Communications*, 2015, **6**, 5963.
13. T. H. Park, S. Yu, S. H. Cho, H. S. Kang, Y. Kim, M. J. Kim, H. Eoh, C. Park, B. Jeong, S. W. Lee, D. Y. Ryu, J. Huh and C. Park, *NPG Asia Materials*, 2018, **10**, 328-339.
14. D.-P. Song, G. Jacucci, F. Dundar, A. Naik, H.-F. Fei, S. Vignolini and J. J. Watkins, *Macromolecules*, 2018, **51**, 2395-2400.
15. M. Heo, H. Cho, J.-W. Jung, J.-R. Jeong, S. Park and J. Y. Kim, *Advanced Materials*, 2011, **23**, 5689-5693.

16. Y. Kang, J. J. Walish, T. Gorishnyy and E. L. Thomas, *Nature Materials*, 2007, **6**, 957-960.
17. J.-H. Lee, C. Y. Koh, J. P. Singer, S.-J. Jeon, M. Maldovan, O. Stein and E. L. Thomas, *Advanced Materials*, 2014, **26**, 532-569.
18. J. K. D. Mapas, T. Thomay, A. N. Cartwright, J. Ilavsky and J. Rzayev, *Macromolecules*, 2016, **49**, 3733-3738.
19. E. Kim, H. Ahn, S. Park, H. Lee, M. Lee, S. Lee, T. Kim, E.-A. Kwak, J. H. Lee, X. Lei, J. Huh, J. Bang, B. Lee and D. Y. Ryu, *ACS Nano*, 2013, **7**, 1952-1960.
20. Y. S. Jung and C. A. Ross, *Advanced Materials*, 2009, **21**, 2540-2545.
21. C. Sinturel, M. Vayer, M. Morris and M. A. Hillmyer, *Macromolecules*, 2013, **46**, 5399-5415.
22. K. W. Gotrik, A. F. Hannon, J. G. Son, B. Keller, A. Alexander-Katz and C. A. Ross, *ACS Nano*, 2012, **6**, 8052-8059.
23. S. H. Kim, M. J. Misner and T. P. Russell, *Advanced Materials*, 2008, **20**, 4851-4856.
24. Y. S. Jung and C. A. Ross, *Nano Letters*, 2007, **7**, 2046-2050.
25. L. Wan, S. Ji, C.-C. Liu, G. S. W. Craig and P. F. Nealey, *Soft Matter*, 2016, **12**, 2914-2922.
26. W. Bai, A. F. Hannon, K. W. Gotrik, H. K. Choi, K. Aissou, G. Liontos, K. Ntetsikas, A. Alexander-Katz, A. Avgeropoulos and C. A. Ross, *Macromolecules*, 2014, **47**, 6000-6008.
27. W. Cao, S. Xia, M. Appold, N. Saxena, L. Bießmann, S. Grott, N. Li, M. Gallei, S. Bernstorff and P. Müller-Buschbaum, *Scientific Reports*, 2019, **9**, 18269.
28. S. Park, Y. Kim, H. Ahn, J. H. Kim, P. J. Yoo and D. Y. Ryu, *Scientific Reports*, 2016, **6**, 36326.
29. K. Takano, T. Nyu, T. Maekawa, T. Seki, R. Nakatani, T. Komamura, T. Hayakawa and T. Hayashi, *RSC Advances*, 2020, **10**, 70-75.
30. G. S. Doerk, R. Li, M. Fukuto and K. G. Yager, *Macromolecules*, 2020, **53**, 1098-1113.
31. C. Jin, B. C. Olsen, E. J. Luber and J. M. Buriak, *Chemistry of Materials*, 2017, **29**, 176-188.
32. P. Mokarian-Tabari, C. Cummins, S. Rasappa, C. Simao, C. M. Sotomayor Torres, J. D. Holmes and M. A. Morris, *Langmuir*, 2014, **30**, 10728-10739.
33. H. Hulkkonen, T. Salminen and T. Niemi, *Soft Matter*, 2019, **15**, 7909-7917.
34. A. Knoll, R. Magerle and G. Krausch, *The Journal of Chemical Physics*, 2004, **120**, 1105-1116.
35. X. Gu, I. Gunkel, A. Hexemer, W. Gu and T. P. Russell, *Advanced Materials*, 2014, **26**, 273-281.
36. R. Lundy, S. P. Flynn, C. Cummins, S. M. Kelleher, M. N. Collins, E. Dalton, S. Daniels, M. A. Morris and R. Enright, *Physical Chemistry Chemical Physics*, 2017, **19**, 2805-2815.
37. G. Nelson, C. S. Drapes, M. A. Grant, R. Gnabasik, J. Wong and A. Baruth, *Micromachines*, 2018, **9**.
38. A. Baruth, M. Seo, C. H. Lin, K. Walster, A. Shankar, M. A. Hillmyer and C. Leighton, *ACS Applied Materials & Interfaces*, 2014, **6**, 13770-13781.
39. X. Cheng, A. Böker and L. Tsarkova, *Polymers*, 2019, **11**, 1312.

40. L. Tsarkova, G. J. A. Sevink and G. Krausch, in *Complex Macromolecular Systems I*, eds. A. H. E. Müller and H.-W. Schmidt, Springer Berlin Heidelberg, Berlin, Heidelberg, 2010, DOI: 10.1007/12_2010_54, pp. 33-73.
41. X. Gu, I. Gunkel, A. Hexemer and T. P. Russell, *Macromolecules*, 2016, **49**, 3373-3381.
42. J. N. Murphy, K. D. Harris and J. M. Buriak, *PLOS ONE*, 2015, **10**, e0133088.
43. X. Gu, Doctoral Thesis, University of Massachusetts Amherst, 2014.
44. K. Koo, H. Ahn, S.-W. Kim, D. Y. Ryu and T. P. Russell, *Soft Matter*, 2013, **9**, 9059-9071.
45. T. P. Lodge, C. Pan, X. Jin, Z. Liu, J. Zhao, W. W. Maurer and F. S. Bates, *Journal of Polymer Science Part B: Polymer Physics*, 1995, **33**, 2289-2293.
46. T. P. Lodge, K. J. Hanley, B. Pudil and V. Alahapperuma, *Macromolecules*, 2003, **36**, 816-822.
47. J. Zhang, D. Posselt, D.-M. Smilgies, J. Perlich, K. Kyriakos, S. Jaksch and C. M. Papadakis, *Macromolecules*, 2014, **47**, 5711-5718.
48. H. Elbs and G. Krausch, *Polymer*, 2004, **45**, 7935-7942.
49. H. N. Sólimo and A. C. Gomez Marigliano, *Journal of Solution Chemistry*, 1993, **22**, 951-962.
50. I. A. Zucchi, E. Poliani and M. Perego, *Nanotechnology*, 2010, **21**, 185304.
51. C. T. Black, C. Forrey and K. G. Yager, *Soft Matter*, 2017, **13**, 3275-3283.
52. C. W. Pester, K. Schmidt, M. Ruppel, H. G. Schoberth and A. Böker, *Macromolecules*, 2015, **48**, 6206-6213.
53. S. Samant, J. Strzalka, K. G. Yager, K. Kisslinger, D. Grolman, M. Basutkar, N. Salunke, G. Singh, B. Berry and A. Karim, *Macromolecules*, 2016, **49**, 8633-8642.
54. L.-Y. Shi, J. Lan, S. Lee, L.-C. Cheng, K. G. Yager and C. A. Ross, *ACS Nano*, 2020, **14**, 4289-4297.
55. P. Müller-Buschbaum, in *Applications of Synchrotron Light to Scattering and Diffraction in Materials and Life Sciences*, eds. M. Gomez, A. Nogales, M. C. Garcia-Gutierrez and T. A. Ezquerra, Springer Berlin Heidelberg, Berlin, Heidelberg, 2009, DOI: 10.1007/978-3-540-95968-7_3, pp. 61-89.
56. M. Y. Paik, J. K. Bosworth, D.-M. Smilges, E. L. Schwartz, X. Andre and C. K. Ober, *Macromolecules*, 2010, **43**, 4253-4260.
57. C. Cummins, A. Gangnaik, R. A. Kelly, D. Borah, J. O'Connell, N. Petkov, Y. M. Georgiev, J. D. Holmes and M. A. Morris, *Nanoscale*, 2015, **7**, 6712-6721.
58. C. Cummins, A. Gangnaik, R. A. Kelly, A. J. Hydes, J. O'Connell, N. Petkov, Y. M. Georgiev, D. Borah, J. D. Holmes and M. A. Morris, *Chemistry of Materials*, 2015, **27**, 6091-6096.
59. M. Khorasaninejad, N. Abedzadeh, J. Walia, S. Patchett and S. S. Saini, *Nano Letters*, 2012, **12**, 4228-4234.
60. J. Walia, N. Dhindsa, M. Khorasaninejad and S. S. Saini, *Small*, 2014, **10**, 144-151.